A Coulomb Stress response model for time-dependent earthquake forecasts

Torsten Dahm[1,2] **and Sebastian Hainzl**[1]

[1]GFZ German Research Centre for Geosciences, Physics of Earthquakes and Volcanoes, Potsdam, Germany

[2]Institute of Geosciences, University of Potsdam, Potsdam, Germany

Key Points:

- We introduce a modified Coloumb Failure seismicity model in which a mean time-to-failure replaces instantaneous triggering.
- The model explains the main features of time-dependent seismicity, including aftershock activity and stress shadow effects.
- As a special case, it includes the Rate-State model solutions but can also handle subcritical stresses and other fracture types.

Corresponding author: Torsten Dahm, dahm@gfz-potsdam.de,tdahm@uni-potsdam.de

Abstract

Seismicity models are probabilistic forecasts of earthquake rates to support seismic hazard assessment. Physics-based models allow extrapolating previously unsampled parameter ranges and enable conclusions on underlying tectonic or human-induced processes. The Coulomb Failure (CF) and the rate-and-state (RS) models are two widely-used physics-based seismicity models both assuming pre-existing populations of faults responding to Coulomb stress changes. The CF model depends on the absolute Coulomb stress and assumes instantaneous triggering if stress exceeds a threshold, while the RS model only depends on stress changes. Both models can predict background earthquake rates and time-dependent stress effects, but the RS model with its three independent parameters can additionally explain delayed aftershock triggering. This study introduces a modified CF model where the instantaneous triggering is replaced by a mean time-to-failure depending on the absolute stress value. For the specific choice of an exponential dependence on stress and a stationary initial seismicity rate, we show that the model leads to identical results as the RS model and reproduces the Omori-Utsu relation for aftershock decays as well stress-shadowing effects. Thus, both CF and RS models can be seen as special cases of the new model. However, the new stress response model can also account for subcritical initial stress conditions and alternative functions of the mean time-to-failure depending on the problem and fracture mode.

Plain Language Summary

One of the most pressing questions in earthquake physics is understanding where and when earthquakes occur and how seismicity is related to stress changes in the Earth's crust. This question is even more important today because humans are increasingly influencing stresses in the Earth by exploiting the subsurface.

So far, two classes of physics-based seismicity models have been used primarily. One assumes instantaneous earthquake occurrence when stress exceeds a threshold, and the other is based on the nucleation of earthquakes according to friction laws determined in the laboratory. Both models are very different in their approaches, have advantages and disadvantages, and are limited in their applicability. In this paper, we introduce a new concept of seismicity models, which is very simple and short to derive and combines the strengths of both previous models, as shown in various applications to human-related seismicity. Both traditional models turn out to be special cases of the new model.

1 Introduction

A seismicity model describes the occurrence of earthquakes, i.e., their origin times, locations, and magnitudes. Because of the complexity of the earthquake processes, nearly all seismicity models use statistical components and only predict the average earthquake rate, respectively the occurrence probability, of earthquakes. Because seismicity models are the backbone of probabilistic seismic hazard assessments, a useful model must be able to represent real seismicity reliably.

Seismicity rates are nearly constant on long temporal and spatial scales at tectonic plate boundaries. This stationarity is related to the steady-state motion of tectonic plates, which leads to temporally constant stressing and seismicity rates. In contrast, on the fault scale, a quasi-periodic recurrence of characteristic events is expected from the classical elastic rebound theory (Reid, 1911). However, such quasi-periodic recurrences of mainshocks have not yet been convincingly documented at plate boundaries (Kagan & Jackson, 1991, 1995; Roth et al., 2017).

On short time scales, earthquake clustering is the most obvious seismicity pattern. Almost every large earthquake is immediately followed by a sequence of smaller magnitude events, so-called aftershocks, clustered around the mainshock rupture. The aftershock rate usually follows the empirical Omori-Utsu relation (Utsu et al., 1995),

$$R(t) \quad = \quad K\,(c+t)^{-p} \tag{1}$$

where c describes the delay of the onset of the aftershock decay with the exponent p. The parameter c is typically in the order of minutes to days, and p scatters around 1. While earthquakes trigger aftershocks overall, they can suppress ongoing activity at some locations, which is explained by the so-called stress-shadowing effect, as e.g. recently shown for the 2019 Ridgecrest sequence (Marsan & Ross, 2021).

Furthermore, aseismic processes are also well-known to trigger time-dependent seismicity. This obviously concerns transient processes at volcanoes (Passarelli et al., 2013; Heimisson et al., 2015), creeping faults inducing seismicity and earthquake swarms (Perfettini & Avouac, 2004; Passarelli et al., 2015), or anthropogenically triggered seismicity related to subsurface use (Becker et al., 2010; Grigoli et al., 2018).

Whether empirical or physical, any seismicity model must be able to reproduce the observed statistical characteristics of time-dependent seismicity. Well-known statistical

models have been established to reproduce short-term aftershock triggering or mainshock recurrences. The epidemic type aftershock sequence (ETAS) model (Ogata, 1988) is widely used to reproduce earthquake clustering. On the other hand, e.g., the Brownian Passage Time model (Matthews et al., 2002) and the stress release model (Vere-Jones, 1978) are used for simulations of quasi-period recurrences of mainshocks at the same fault. Those statistical models can successfully describe either aftershock patterns or seismic cycles and stress-shadowing effects but fail to model both. In contrast, seismicity models considering explicitly the real stress changes can do it. Those physics-based seismicity models are additionally an indispensable prerequisite for understanding earthquake triggering and can make predictions of time-dependent earthquake rates outside the range of previous observations. Among the class of physics-based seismicity models, two models are widely used to study seismicity patterns: (1) the Coulomb Failure (CF) model, and (2) the rate-state (RS) model based on a laboratory-derived constitutive rate-and-state dependent friction law (Dieterich, 1994). Both models were developed for shear cracks and use time-dependent Coulomb stress changes as input (in a Coulomb stress approximation).

The CF model assumes instantaneous earthquake triggering when the absolute Coulomb stress exceeds a static strength threshold. The predicted earthquake rate correlates linearly with the stressing rate if a pre-existing population of potential faults with uniformly distributed stress is assumed, as long as stress increases. In contrast, a complete absence of seismicity is expected during periods of stress shadows after stress drops. Because a retarded triggering of earthquakes is not considered, the CF model cannot explain aftershocks solely by the mainshock stress changes. It requires the involvement of triggered aseismic slip, so-called afterslip, to reproduce the characteristics of aftershock sequences (Perfettini & Avouac, 2004).

The RS model posited by Dieterich (1994) is based on the assumption that fault slip is described by the constitutive rate-and-state dependent friction law observed in laboratories. It assumes that frictional instabilities occur in a population of fault patches in a way that the earthquake rate is initially constant due to constant tectonic stressing. In contrast to CF, it depends only on the stress change and not on the absolute stresses. RS explains, like CF, a constant earthquake rate for constant stressing and a rate decrease during periods of stress shadows. Additionally, it reproduces an Omori-Utsu type aftershock decay following a positive stress step. While the CF model has additional to

the stress loading and threshold only one model parameter, the RSM has three model parameters. Its derivation is quite complex and uses several additional intrinsic assumptions. In a recent study, Heimisson and Segall (2018) revisited the RS theory with a different assessment and interpretation of the various model assumptions.

The new effective media model developed in this study is a modified Coulomb failure model, which accounts for delayed nucleation of both tensile and shear cracks, simply by a stress-dependent mean time-to-failure. We first introduce the concept of the effective media approach and the modified Coulomb failure model, derive the theoretical implications, and then discuss the model predictions in context with some field observations for induced seismicity, aftershock decays, and stress shadow effects in comparison to the established CF and RS models.

2 Time-dependent stress response model (TDSR)

2.1 Concept

The earthquake rate is the number of events in a given volume and time interval with magnitudes above a completeness value M_c. We define an elementary rock volume V that undergoes a uniform time-dependent change in stress or pressure. The volume is cut through by pre-existing faults and fractures, which may possibly support an earthquake rupture (Fig. 1a for illustration). The faults or neighboring rock contains local stress peaks ("sources") of uneven areas of varying size, which may be viewed as asperities. In the effective medium approach, the interaction of the sources is considered by replacing the rock volume with a substitute medium with average properties (effective modules) depending on the fault density (Dahm & Becker, 1998). The distribution of average background stress (represented by principal effective stresses σ_1' and σ_3') and Coulomb stresses at the individual sources can be visualized in a Mohr Coulomb diagram (Fig. 1b). We assume that, although the absolute stress at each source within V can vary and also be different from the ambient background stress, the change in Coulomb stress is assumed to be equal. For instance, the Coulomb stress changes $\Delta\sigma$ may occur by a redistribution of stress in V after a major earthquake, by other types of internal aseismic dislocation sources beside V or by pore pressure changes in the rock volume itself.

In the CF model, an earthquake is instantaneously triggered when the Coulomb stress σ_c at the source exceeds the inherent cohesive strength S_0. For a constant and uni-

form stressing rate $\dot{\sigma}_c$, the time-to-failure t_f for a source is in this case simply given by $t_f = \zeta/\dot{\sigma}_c$ with $\zeta = S_0 - \sigma_c$ being the difference between strength threshold and the actual Coulomb stress at the source. Thus, a constant rate r_0 results in the CF model for a uniform pre-stress density distribution $\chi(\zeta) = (r_0/\dot{\sigma}_c)H(\zeta)$, where H is the Heaviside function ($H(x) = 1$ for $x \geq 0$ and 0 else).

While the deterministic failure criterion of the CF model is simple and thus attractive, it is an oversimplification. Instead of a fixed threshold and instantaneous triggering, instabilities are realistically expected to occur at various stress levels with stress-dependent nucleation times for instabilities to grow into seismic ruptures. Based on experimental data on subcritical crack growth, a popular equation for the mean time-to-failure $\bar{t}_f$ is an exponential function according to

$$\bar{t}_f \quad = \quad t_0 \, e^{\frac{\zeta}{\delta\sigma}} \tag{2}$$

The constant t_0 is the mean delay time for a critically stressed source ($\zeta = 0$) and can be assumed very small. The parameter $\delta\sigma$ controls the increase of $\bar{t}_f$ with ζ and is in our study denoted as skin parameter. In the limit of $\delta\sigma \rightarrow 0$, the time-to-failure becomes ∞ for $\zeta > 0$ and 0 for $\zeta < 0$; thus leading to the CF model.

The exponential law has been suggested for both quasi-static crack propagation of tensile (Aktinson, 1984) and shear cracks in brittle rock (Ohnaka, 2013) if ζ is either interpreted as a function of the stress intensity factor or the difference between strength and Coulomb stress, respectively. For instance, Scholz (1968) used the exponential form of $1/\bar{t}_f$ to explain the mechanism of creep in brittle rock. The same law has been used to explain crack growth in ceramics (Wiederhorn et al., 1980) or the number of acoustic emissions under creep (e.g., Ohnaka (1983) and references therein). We follow Scholz (1968) and Ohnaka (2013) and define ζ by $S_0 - \sigma_c$. However, the concept can be equally well be applied to tensile crack seismicity or other forms of the mean decay times.

Given the mean time-to-failure $\bar{t}_f$, the mean failure rate for N sources is given by $N/\bar{t}_f$. Thus, the distribution of sources at the different stress levels has to be considered to calculate the total event rate of the volume. This time-dependent density distribution of sources is defined by $\chi = \chi(\zeta, t)$ and the total rate at time t becomes

$$R(t) \quad = \quad \int_{-\infty}^{\infty} \frac{\chi(\zeta, t)}{\bar{t}_f(\zeta)} \, d\zeta \, , \tag{3}$$

where $\bar{t}_f(\zeta)$ is given by Eq. (2) and independent of time. In order to use this relation for rate forecasts, the evolution of $\chi(\zeta, t)$ is needed. To solve it analytically or numerically, we use the following assumptions and simplifications:

1. Each source in V is loaded by the same stress and acts independently (effective media approach)
2. In addition to external loading, each source is subject to static fatigue described by Eq. (2).
3. Each source fails only once during a simulation, i.e., the stress drop ΔS is significantly larger than the loading stress during the simulation, and failed sources can be removed from the distribution of available sources.
4. For simplifying the following analytical calculations, we ignore that ζ is limited by the maximum value S_0. This assumption holds for $\delta\sigma \ll \Delta S$.

2.2 Analytic solutions

The model forecasts can be analytically derived for some simplified stress scenarios. These solution can be all derived from the total time derivative of χ being equal to the negative event rate, namely

$$\frac{\mathrm{d}\chi(\zeta,t)}{\mathrm{d}t} = \frac{\delta\chi(\zeta,t)}{\delta t} + \frac{\delta\chi(\zeta,t)}{\delta\zeta}\frac{\mathrm{d}\zeta}{\mathrm{d}t} = -\chi(\zeta,t)\,/\,\bar{t}_f(\zeta)\,. \tag{4}$$

The detailed derivations of the following solutions can be found in the Appendix A1.

2.2.1 Uniform initial distribution with constant loading

For the case of an initially uniform stress distribution for $\zeta > \zeta_{\min}$ at $t = 0$, i.e. $\chi(\zeta, 0) = \chi_0\, H(\zeta - \zeta_{\min})$ and a constant stressing rate $\dot{\sigma}_c$ for times $t > 0$, the time-dependent seismicity rate is

$$R(t) = \chi_0 \dot{\sigma}_c \frac{1 - e^{\frac{\delta\sigma}{t_0 \dot{\sigma}_c}\left(1 - e^{-\frac{\dot{\sigma}_c\, t}{\delta\sigma}}\right) e^{-\frac{\zeta_{\min} - \dot{\sigma}_c\, t}{\delta\sigma}}}}{1 - e^{-\frac{\dot{\sigma}_c\, t}{\delta\sigma}}}\,. \tag{5}$$

The solution can be compared to the rate expected in the CF and RS model. In the CF model, $R(t) = \chi_0\, \dot{\sigma}_c\, H(t - \zeta_{\min}/\dot{\sigma}_c)$, i.e., the CF model predicts a sudden onset of a constant seismicity rate at time $t = \zeta_{\min}/\dot{\sigma}_c$. In contrast, the original RS model of Dieterich (1994) always assumes a stationary background seismicity ($r \equiv r_0$) as starting condition and thus cannot deal with a subcritical initial stress state. Heimisson et al. (2022)

extended the RS-framework for subcritical initial stress states ($RS_{subcrit}$). The solution of their Eq. (1) for $\Delta S_c = \zeta_{min}$ and a constant stressing rate $\dot{\sigma}_c$ yields $R(t) = r_0\, H(t - \zeta_{min}/\dot{\sigma}_c)$, i.e., an instantaneous onset of a constant rate at $t = \zeta_{min}/\dot{\sigma}_c$ as the CF model.

2.2.2 Stationary seismicity

The stress distribution associated to a constant seismicity rate $R(t) = r_0$ for a given stressing rate $\dot{\sigma}_c$ is given by

$$\chi_s(\zeta) = \frac{r_0}{\dot{\sigma}_c} \exp\left(-\frac{\delta\sigma}{t_0 \dot{\sigma}_c}\, e^{-\frac{\zeta}{\delta\sigma}}\right). \tag{6}$$

Here, the subscript in χ_s is used to denote that this distribution is stationary, i.e., time-independent. The prefactor $\chi_0 = r_0/\dot{\sigma}_c$ expresses the susceptibility of the rock volume.

2.2.3 Stress step

Here it is assumed that the initial pre-stress distribution is given by χ_s related to constant stressing and seismicity rate, $\dot{\sigma}_c$ and r_0, respectively. A stress step $\Delta\sigma_c$ is applied at time $t = 0$ followed by a loading with constant stressing rate $\dot{\sigma}_{c,a}$ at $t > 0$. The seismicity rate is in this case given by

$$R(t) = \frac{r_0 \frac{\dot{\sigma}_{c,a}}{\dot{\sigma}_c}}{\left(\frac{\dot{\sigma}_{c,a}}{\dot{\sigma}_c} e^{-\frac{\Delta\sigma_c}{\delta\sigma}} - 1\right) e^{-\frac{\dot{\sigma}_{c,a}\, t}{\delta\sigma}} + 1} \qquad \text{for} \quad \dot{\sigma}_{c,a} \neq 0 \tag{7}$$

and

$$R(t) = \frac{r_0}{e^{-\frac{\Delta\sigma_c}{\delta\sigma}} + \frac{\dot{\sigma}_c}{\delta\sigma}\, t} \qquad \text{for} \quad \dot{\sigma}_{c,a} = 0. \tag{8}$$

For positive stress steps, the second equation is identical to the Omori-Utsu law Eq. (1) with $p = 1$, $c = \frac{\delta\sigma}{\dot{\sigma}_c} \exp\left(-\frac{\Delta\sigma_c}{\delta\sigma}\right)$, and $K = \frac{r_0\, \delta\sigma}{\dot{\sigma}_c}$. While the CF model cannot predict Omori-type aftershocks, both equations are identical to the solutions of the RS-model for the same conditions, namely Eq. (12) and (13) of Dieterich (1994) with $A\sigma \equiv \delta\sigma$, $r \equiv r_0$, $\dot{\tau}_r \equiv \dot{\sigma}_c$, and $\dot{\tau} \equiv \dot{\sigma}_{c,a}$.

2.2.4 Changing stressing rates

The solution for a changing stressing rate from $\dot{\sigma}_c$ for $t \leq 0$ to the new constant stressing rate $\dot{\sigma}_{c,a}$ for $t > 0$ can be directly derived from Eq. (7) by setting $\Delta\sigma_c = 0$, yielding

$$R(t) = \frac{r_0}{\left(1 - \frac{\dot{\sigma}_c}{\dot{\sigma}_{c,a}}\right) e^{-\frac{\dot{\sigma}_{c,a}\, t_b}{\delta\sigma}} + \frac{\dot{\sigma}_c}{\dot{\sigma}_{c,a}}}. \tag{9}$$

A ramp-like excitation in stress, or a box-car stressing rate with duration t_b and $\dot{\sigma}_c$ for $t < 0$ and $t > t_b$ and $\dot{\sigma}_{c,a}$ elsewhere, can be constructed from (9) by

$$R(t) \quad = \quad R_1([0 : t_b]) + R_2([t_i : \infty] - t_b)\,, \tag{10}$$

where $t_i = -\dfrac{\delta\sigma}{\dot{\sigma}_c} \ln\left(1 - e^{-\frac{\dot{\sigma}_{c,a}\, t}{\delta\sigma}}\right)$ and R_1 given by (9) and R_2 by (9) with interchanging $\dot{\sigma}_c$ and $\dot{\sigma}_{c,a}$.

3 Applications

While the analytic solutions (Eqs. 5-9) can be used for simple stressing histories, the integral in Eq. (3) must be solved numerically for more complex cases. The numerical model implementation is straightforward, and the simple algorithm, which we used for the simulations presented in this work, is provided in Appendix A2.

3.1 Synthetic examples

The following synthetic case studies are used to illustrate the response to some generic setups.

3.1.1 Subcritical uniform pre-stress distribution

Figure 3(a) shows the TDSR forecasts for the case of a uniform pre-stress distribution and constant loading $\dot{\sigma}_c$. The numerical simulations of the TDSR model exactly resemble Eq. (5). The three analyzed $\zeta_{\min}$ values of 0, 3, and 6 lead to different responses. For $\zeta_{\min} = 0$, the rate decays with time until it reaches the stationary seismicity rate $r_\infty = \chi_0\, \dot{\sigma}_c$. In contrast, the seismicity rate is initially much lower than r_∞ and only starts to accelerate and converge with some delay for $\zeta_{\min} > 0$. In comparison to the predictions of CF and $\mathrm{RS}_{\mathrm{subcrit}}$, which are both identical for this setup, the onset of the seismicity is smooth and occurs earlier. The accelerated seismicity already reached the steady-state when the other models predicted the sudden onset. Thus, for a fixed onset time of the seismicity, the estimated $\zeta_{\min}$ value for TDSR will be larger than for CF and $\mathrm{RS}_{\mathrm{subcrit}}$ (e.g., see the application to Groningen in Sec. 3.2.1).

241 ### *3.1.2 Aftershock triggering*

242 The TDSR model with stationary pre-stress distribution (Eq. 6) leads to Omori-
243 type aftershock sequences with $p = 1$ for positive stress steps at $t = 0$. Figure 3(b)
244 shows the immediate rate increase in a double logarithmic plot as a function of time af-
245 ter the stress step, where the stressing rate remains constant, i.e., $\dot{\sigma}_{c,a} = \dot{\sigma}_c$. The nu-
246 merical simulations exactly match Eq. (7). It is important to note that (i) the aftershock
247 rate is directly proportional to the background rate r_0, (ii) the maximum seismicity rate
248 at $t = 0^+$ is $r_0 \exp(\Delta\sigma_c/\delta\sigma)$, (iii) the duration of the aftershock decay is given by $t_a \equiv$
249 $\delta\sigma/\dot{\sigma}_c$, and (iv) the time delay until the onset of the $1/t$ decay (c-value in Eq. 1) depends
250 on the stress step. The larger the step, the shorter the delay.

251 ### *3.1.3 Stress shadowing*

252 The seismicity rate is commonly assumed to decrease during periods (so-called stress
253 shadows) in which the absolute stress dropped below its previous maximum value. This
254 stress shadow effect is commonly known as Kaiser effect. To illustrate the response of
255 the TDSR model to stress shadows, we run simulations with stationary pre-stress dis-
256 tributions. Figure 4(a) shows the result for sudden stress drops ($\Delta\sigma_c < 0$), which are
257 also described by Eq. (7). For instance, a volume of rock on the rupture plane of a large
258 earthquake may experience a co-seismic negative stress step when the rupture front has
259 passed by. The TDSR model predicts similar to the RS model that the seismicity rate
260 drops instantaneously in this case from r_0 to $r_0 \exp(\Delta\sigma_c/\delta\sigma)$ and then recovers slowly
261 until it reaches the background level at approximately $6\,t_a$. Thus, the memory for stress
262 drops is a few times larger than for positive stress steps, i.e., aftershock sequences. In
263 contrast, the CF model (i.e., the TDSR model in the limit for $\delta\sigma \to 0$) predicts an ab-
264 solute quiescence of length $t_a\,|\Delta\sigma_c|/\delta\sigma$ followed by an instantaneous recovery of the back-
265 ground rate. Similarly, for cyclic loading shown in Fig. 4b, the TDSR model predicts smooth
266 transitions from almost zero rates to high activity and vice versa, while CF shows sharp
267 transitions.

268 ## 3.2 Applications to real data

269 Analytic solutions and simple synthetic model runs are helpful to clarify and demon-
270 strate general model properties, but the ultimate goal of any seismicity model is the ap-

plication to real data. In the following, we briefly discuss some examples of TDSR applications to induced and natural seismicity, which are related to the synthetic case studies.

3.2.1 Groningen

The Groningen field, Netherlands, is one of the largest gas reservoirs in the world. The gas production started in 1963, but the first earthquake related to gas extraction was only detected in 1991. At that time, the reservoir pore pressure dropped already approximately 10 MPa, related to a rock stress increase of similar magnitude, generally taken as evidence that before production, most Groningen faults were far from critical stress (Candela et al., 2018). Since 1991, more than 350 earthquakes with magnitude $M_L \geq 1.5$ have been recorded.

The occurrence of felt earthquakes accompanying the gas production initiated dense instrumentation, numerous field studies, and the development and application of many seismicity models for explaining and quantifying the observed seismicity, see the recent review of Kühn et al. (2022). For example, a CF model version was developed by Bourne and Oates (2017) and Bourne et al. (2018) assuming that the stresses at the activated faults are in the tail of the pre-stress distribution. The latter assumption was used to apply extreme value statistics to explain the observed non-linear response to the stress changes. Furthermore, different RS model implementations have been applied to Groningen, among others Dieterich's model (RS) by Richter et al. (2020) and the subcritical RS model ($\mathrm{RS_{subcrit}}$) by Heimisson et al. (2022). These model applications were based on estimated stress changes in space and time, including available fault information. Here we do not want to compete with those detailed studies but only want to demonstrate the potentials of the TDSR model and leave a detailed analysis to future work. For simplification, we only consider the annual changes of the mean pore pressure in the field and assume that Coulomb stress changes are proportional to the size of the pore pressure drop.

We compare the TDSR forecasts with the corresponding results of the CF, RS, and $\mathrm{RS_{subcrit}}$ models. To reduce the number of free model parameters, we constrained the pre-factors by the condition that the total number of forecasted earthquakes equals the observed events in 1991-2021. With this constraint, CF considering continuous tectonic

stressing has no free parameter, CF assuming a subcritical initial stress state ($CF_{subcrit}$) has one (ζ_{min}), RS has two ($A\sigma$ and $\dot{\sigma}_c$), and $RS_{subcrit}$ has three parameters ($A\sigma, \dot{\sigma}_c$, and ζ_{min}). For both models, $CF_{subcrit}$ and $RS_{subcrit}$, the stress gap had to be equalized by the gas production at the time when the seismic activity started; thus, we set ζ_{min}=8.5 MPa, which was equalized just before the first observed earthquakes in 1991. Furthermore, we set $A\sigma$=1 MPa which is in the range of the results of Richter et al. (2020). The free parameters of the TDSR model depend on the assumed initial conditions. Assuming a constant background seismicity, i.e. a stationary TDSR pre-stress distribution according to Eq. (6), leads to forecasts which are independent of t_0 and identical to the RS model for $\delta\sigma = A\sigma$ using the same stressing rate $\dot{\sigma}_c$. However, the TDSR model also works for subcritical stress conditions with zero background stressing. Instead of $\dot{\sigma}_c$, the model depends on t_0 and the parameters required to characterize the pre-stress condition; e.g., ζ_{min} for a uniform pre-stress distribution, or the mean $\bar{\zeta}$ and standard deviation ζ_σ for a Gaussian distribution.

Figure 5(b) shows the results of the TDSR model in comparison to the other models, where we set the remaining free parameters in order to fit the observed annual rates of earthquakes with magnitudes larger than 1.45, i.e., the estimated completeness magnitude. We find that

- The CF model with uniform pre-stress conditions cannot fit the observations, neither for critical nor for subcritical conditions.
- TDSR and RS assuming an initially constant background seismicity rate lead to identical fits. For a reasonable data fit, the stressing rate must be extremely low ($\dot{\sigma}_c$=3.3 Pa/year in Fig. 5).
- $RS_{subcrit}$ leads to almost the same result as RS but with a significantly larger stressing rate, namely 17 kPa/year for the same $A\sigma$ value.
- To get similar fits, the pre-stress conditions in the TDSR model depend on t_0; the shorter t_0, the larger the pre-stress gaps, or vice versa. For a mean nucleation time at critical stress of $t_0 = 10^{-4}$ years (≈53 min), the stress gap is significantly larger (ζ_{min}=22 MPa, respectively $\bar{\zeta}$=24.5 MPa) compared to 8.5 MPa estimated by $CF_{subcrit}$ and $RS_{subcrit}$.
- The shape of the ongoing seismicity rate decay depends strongly on the assumed pre-stress distribution shown in Fig. 5(a). While the predictions of the RS mod-

els and the TDSR model either with background stressing or uniform pre-stress distribution behave similarly, the decay is much steeper if a Gaussian distribution of sources is assumed. In the latter case, the depletion of available sources starts to dominate the activity, which might have important implications for seismic hazard studies.

3.2.2 Fits to aftershock sequences

Important applications of seismicity models are forecasts of aftershock sequences because aftershocks can sometimes be very destructive and deadly. Major aftershock sequences are typically observed at tectonic plate boundaries, where a constant background stressing rate can be assumed for loading the fault system. Thus, in the absence of any additional information, a constant background rate as initial condition is reasonable in this case. Then, as discussed before, the TDSR model forecasts are identical to the RS model with $\delta\sigma = A\sigma$.

To estimate the $\delta\sigma$-parameter for aftershock sequences, we can thus make use of existing RS applications based on detailed slip models leading to varying stress steps in space. Such sophisticated model applications exist, among others, for the 1992 M7.2 Landers sequence (Hainzl, Steacy, & Marsan, 2010), 2004 M6 Parkfield and the 2011 M9 Tohoku sequences (Cattania et al., 2014), the 2010-2012 Canterbury sequence (Cattania et al., 2018), and the 2016–2017 Central Italy earthquake cascade (Mancini et al., 2019). The studies show good fits with $A\sigma$, i.e. $\delta\sigma$, in the range of 0.01–0.1 MPa.

3.2.3 Examples of stress shadows effects

Induced earthquakes are well suited as case studies for stress shadows when they are associated with a controlled, short-term change in Coulomb stress, for instance related to periodic fluid injections in basement rocks or cyclic thermal loading of a mine gallery.

KTB experiment

The first example treats a sequential fluid production and injection experiment in 4 km depth at the German Continental Deep Drilling site (KTB) in Windischeschenbach, Bavaria, Germany (Fig. 6). The KTB consists of two accessible boreholes drilled 200 m from each other into crystalline rock, the 4000 m deep pilot well and the 9100 m deep

main well (Kümpel et al., 2006). Two distinct fault systems cut through the hydraulically connected wells. The hydraulic experiment started in June 2002 with a one-year production of 22,300 m^3 of saline water of 120°C from the open section of the pilot well between 3850 m and 4000 m depth (Kümpel et al., 2006). The drawdown of the fluid level in the pilot well reached 605 m at the end of the production phase in June 2003. The fluid level in the main well gradually dropped from zero to 50 m below the surface during the production phase, indicating a hydraulic connection between the two wells likely originating at a leakage in the casing of the main well between 5200 and 5600 m depth (Grässle et al., 2006). In June 2004, after a one-year recovery phase following the production, an injection experiment was conducted until April 2005. Overall, 84,500 m^3 of freshwater, about four times the produced volume, was re-injected during ten months in the same open-hole section of the pilot hole. Although the injection rate was more or less constant between 185 and 196 l/min, the wellhead pressure varied between 9 and 12 MPa (Kümpel et al., 2006). In October 2004, 114 days after the start of the injection, the main hole became artesian with a rate of $\sim 6.9{\cdot}10^{-4}$ m^3/min (~ 1 m^3/day) (Kümpel et al., 2006). Because of the hydraulic connection between the two wells, the water level in the main well directly measured the time-dependent pressure change ΔP_f at the leakage point at a depth of $\sim$ 5500 m. Using this and other information on the local hydraulic structure, Grässle et al. (2006) modeled the pressure field between the two wells using a 3D diffusivity model. As we are interested in pressure changes only, our modeling approach is simpler and involves a poroelastic diffusion modeling in full space (Rudnicki, 1986). A hydraulic diffusivity of $D = 0.033$ m^2/s is found to explain the ΔP_f variations at the open section of the main well (Fig. 6d). Here we used a rigidity of $1\,GPa$, a drained and undrained Poisson ratio of 0.25 and 0.3, respectively, and a Biot-Willies constant of $\alpha = 0.1$. The model is used to extrapolate into the artesian phase during injection, where no water level measurements were possible.

Induced seismicity was recorded at a borehole geophone in the main hole (3 components, 15 Hz, 1000 Hz sampling rate, clamped at different depths between 1950 m and 3000 m) and a surface array of five short-period stations in a distance of up to 3 km from the main hole (Shapiro et al., 2006; Haney et al., 2011). The largest 104 induced earthquakes had magnitudes between $-1.8 \leq M_L \leq 1$ and could be accurately located from both networks. The events occurred between 3.3 and 4.9 km depth near the main well (Fig. 6a,c). The borehole geophone was very close to the center of the cluster. In total,

about 3040 event arrivals were detected from which 2404 clustered micro-earthquakes were located with magnitudes $M_L \geq -3.8$ and with a magnitude of completeness of $M_c \sim -2.75$ (Haney et al., 2011). We use a more conservative limit of $M_c = -2.3$ (Fig. 6e).

The first seismicity occurred when the pore pressure at depth in the main hole reached and exceeded the original level from before 2002 (Fig. 6d). We performed simulations to verify whether TDSR can explain the onset and time evolution of the earthquake rate. We assume that $\mu\Delta P_f$ dominates the Coulomb stress change, where μ is the friction coefficient. Our estimated Coulomb stress change thus covers the full experiment from the pumping over the recovery to the injection phase over altogether 1200 days. As the experiment took so long, it poses a unique opportunity to test stress shadow models.

The stress state at KTB is known to be critical, where small stress perturbations triggers earthquakes (Zoback & Harjes, 1997). Thus, we assume a stationary pre-stress distribution according to Eq. (6). The majority of the activity occurred with a distance between 300 m and 600 m to the injection point, thus we averaged the TDSR-response function in this distance range and calibrated the resulting curve by the total number of observed earthquakes with magnitude exceeding M_c. Figure 6f shows the result earthquake rates for $\delta\sigma/\mu$=0.9, 1.0, an 1.1 MPa using a tectonic stressing rate of $\dot{\sigma}_c$=30 Pa/year. Assuming $\mu \approx 0.5$, we estimate slightly larger $\delta\sigma$-values as for aftershock sequences. The onset and non-linear increase of the observed seismicity rate are well explained.

Morsleben

The second example involves the controlled refilling of an about 80 years old, abandoned salt gallery in the Morsleben mine, Germany, in a depth of 300 m below the surface. The salt-cement was backfilled continuously for approximately 182 days, with the exception of weekends and holidays, resulting in periodic variations of thermally induced Coulomb stresses in the roof region of the gallery. The periodic stress variations induced microseismic activity, so-called acoustic emissions in the frequency range of 1-20 kHz. A detailed description of the mine, the salt rock, the seismic monitoring system, and the location and magnitude estimation can be found in Köhler et al. (2009) and Becker et al. (2010). The high-quality catalog of AE events comprises hundreds of thousands of high-quality events which occurred in a confined volume above the backfilled gallery. Coulomb stress changes in the roof region were calculated with a 2D thermo-elastic finite element method using temperature measurements as boundary conditions (Becker et al., 2010).

The observed AEs showed a high correlation to positive Coulomb stress changes but also clear stress shadow effects (Becker et al., 2010). Figure 7(a) and (b) shows a map-view and cross-section of the mine structure together with the seismic network and the AEs. Figure 7(c) shows the $\Delta\sigma_c$ changes in the selected rock volume of $V = 15\,\mathrm{m}\,x\,15\,\mathrm{m}\,x10\,\mathrm{m} \sim 2250\ \mathrm{m}^3$ in the southern region as defined in Becker et al. (2010). In this volume, $\Delta\sigma_c$ changes almost in phase with little spatial variations.

We applied the TDSR model using the modeled $\sigma_c(t)$. In contrast to the KTB case, the pre-stress is expected to be subcritical in the salt mine and tectonic stressing is zero. Thus, we assume a subcritical, uniform pre-stress distribution at the starting time, i.e., $\chi(\zeta) = \chi_0 H(\zeta - \zeta_{\min})$. The susceptibility χ_0 is determined by the condition that the total number of the predicted events should equal the observed ones. The remaining model parameters are $\zeta_{\min}, t_0$, and $\delta\sigma$. For simplicity, we set $t_0 = 0.01$ days but noticed that similar results are obtained for other t_0 values if $\zeta_{\min}$ is rescaled. Thus, the two parameters $\zeta_{\min}$ and $\delta\sigma$ determine the shape of the predicted model rate.

Fig. 7(d) shows the comparison of the observed rates with the model forecasts for three skin parameters, $\delta\sigma = 0.3$ MPa, 0.4 MPa, and 0.5 MPa, and corresponding $\zeta_{\min}$-values. TDSR shows a good fit to the data. The onset and width of the peaks as well as the relative heights of the cycles are well reproduced in all three cases. However, further increasing or lowering $\delta\sigma$ leads to underestimating or overestimating the rate response to $\sigma_c(t)$ cycles. Thus, we can conclude that $\delta\sigma$ is in the range between 0.3 and 0.5 MPa.

4 Discussion

Depending on the objective and application, various seismicity models are presently used, including statistical and physics-based models or combinations of both. A recent review of the strength and weaknesses of different models applied to the specific case of the Groningen gas field is given in Kühn et al. (2022). The most popular physics-based seismicity models are the variants of the CF and the RS models, while the ETAS model is the standard statistical model for describing short-term earthquake clustering.

The newly introduced TDSR model can be seen as a generalization of both physics-based CF and RS models. Specifically, the CF model is the limit of TDSR for $\delta\sigma \to 0$, as discussed in Sec. 2.1. Thus, CF is the special case of the TDSR for a vanishing skin

parameter. Although CF can explain the occurrence of stress shadows (Kaiser effect), its prediction of sudden onsets and ends of total quiescences is not realistic. Furthermore, CF cannot explain Omori-type aftershock triggering following sudden stress steps. This shortcomings vanish in the TDSR model with $\delta\sigma > 0$.

The relation of the TDSR model to RS is more complicated than to CF. As we have shown in this paper, the analytic and numerical results of RS are identical to the results of the TDSR model for the special case that the initial stress is in steady-state related to background stressing. In particular, the original RS model, as formulated by Dieterich (1994) and Heimisson and Segall (2018), uses the pre-condition $\dot{\sigma}_c = \text{const} > 0$ and was not developed to study scenarios under $\dot{\sigma}_c = 0$. The assumption of initial steady-state conditions leads to a constrained pre-stress distribution. Heimisson et al. (2022) recently extended the RS approach to allow for subcritical starting conditions but still assumes non-zero background stressing rates, manifested in the model parameter $t_a = A\sigma/\dot{\sigma}_c$. In contrast, TDSR can be applied to arbitrary initial pre-stress conditions and does not generally require a constant background stressing rate. Simulations with $\dot{\sigma}_c \approx 0$ can be of particular interest for anthropogenic seismicity occurring in intraplate regions as in the case of our example in Morsleben; or, likewise, after driving a tunnel into a rock mass not subject to tectonic strain and stress rates.

While the predicted seismicity rates are identical for initial steady-state conditions related to $\dot{\sigma}_c > 0$, the concepts of both TDSR and RS are very different. The RS model assumes an infinite population of nucleation sites, where slip on each patch is described by a rate- and state-dependent constitutive law derived from friction experiments in the laboratory (Dieterich, 2007). For each of the isolated and non-interacting patches, a simplified spring slider model under friction is used to characterize the nucleation process by an interval of self-driven, accelerated slip, according to the aging law suggested by Ruina (1983). An earthquake is assumed to occur when the slip rate becomes very large or infinity. Finally, the seismicity model only depends on stress changes and not on absolute stress. In contrast, the TDSR model has a direct link to the absolute stress level by assuming that mean time-to-failure $\bar{t}_f$ is a function of the absolute stress. We use an exponential function (Eq. 2) that has been widely used to study subcritical crack growth and brittle failure in geological materials, both under tensional stresses (see review in Aktinson (1984)) and compressional (shear) stresses (Scholz, 1968; Ohnaka, 1983). Thus, it seems enigmatic why RS and TDSR result in the same solutions (for $\dot{\sigma}_c > 0$), despite

the contrasting concepts. The underlying reason might be that the RS approach also leads intrinsically to an exponential dependence of the time-to-failure on the absolute stress level. The derivation shown in Appendix Appendix B also provides the relation between t_0 and the microscopic and constitutive RS parameters. However, in general, the TDSR approach may also be used with other functional dependencies of $\bar{t}_f$ on stress, e.g., to study the seismicity of tensile cracks.

The simplicity of the TDSR model might offer additional possibilities. By explicitly tracking the stress distribution of sources, possible dependencies of the frequency-magnitude distribution on the stress state can be directly implemented. Particularly, the Gutenberg-Richter b-value is expected to depend on the absolute stress, with lower values (increased average magnitudes) for higher stress levels (Scholz, 2015). Such relations can be simply implemented and tested in the TDSR approach.

In contrast to the discussed physics-based models, the ETAS model does not rely on stress or stress changes at all. It is a statistical approach to describe short-term clustering of seismicity, particularly aftershock occurrence. For this purpose, it considers a stationary background rate and uses empirical relations to describe clustering: (i) the temporal aftershock decay (Omori-Utsu law), (ii) the observed exponential dependence of the aftershock productivity on the mainshock magnitude, and (iii) the spatial decay of the aftershock density with distance to the mainshock. Although, the physics-based model also derives all three properties (shown here and in Hainzl, Brietzke, and Zoeller (2010)) there are important differences: Firstly, the background rate is additive in ETAS, while it is multiplicative in the physics-based models. It means that the short-term aftershock rate depends only on the mainshock magnitude in the ETAS model, while it also scales with the background rate in TDSR and RS. Secondly, the aftershock decay is infinite in the ETAS model, while it has a characteristic duration $t_a = \delta\sigma/\dot{\sigma}_c$ in TDSR, which is better fitting empirical data on average (Hainzl & Christophersen, 2017). Thirdly, the c-value of the Omori-Utsu relation is not, as in ETAS, a constant but depends on the stress step and is thus space-dependent in the TDSR model. Finally, and maybe most importantly, ETAS only accounts for activation and cannot explain stress shadows. The minimum rate at any location is the tectonic background rate. Despite these unphysical characteristics, the ETAS model mostly outperformed RS implementations in retrospective tests for major aftershock sequences (Woessner et al., 2011; Cattania et al., 2018). The reason is likely that the physics-based models suffer from the large uncer-

tainties of the mainshock-induced stress changes (Hainzl et al., 2009) and ETAS additionally accounts for secondary aftershock triggering by smaller magnitude events. However, in the case of anthropogenic seismicity, earthquake-earthquake triggering is less important, and seismicity is largely driven by the time-dependent stress changes related to the human activity. In the latter case, the physics-based models are superior, and ETAS might only be used to explain additional earthquake-earthquake triggering (Kühn et al., 2022).

5 Conclusions

Assuming simply an exponential dependence of the mean time-to-failure on the absolute stress, the proposed time-dependent stress response (TDSR) model can explain the most important characteristics of seismicity, namely aftershock triggering and stress shadowing. It is a generalization of the deterministic Coulomb Failure (CF) model where earthquakes nucleate instantaneously when the strength threshold is exceeded. Furthermore, TDSR leads to the same analytic and numerical solutions as the well-known rate- and state (RS) model for the special case of steady-state initial pre-stress conditions related to a constant background rate. RS is based on a completely different concept, exploiting a rate- and state-dependent constitutive law derived from laboratory friction experiments. However, TDSR is not limited to initial steady-state conditions and can also simulate seismicity with subcritical initial conditions and zero tectonic stressing. The latter might be of particular interest for applications to human-induced seismicity.

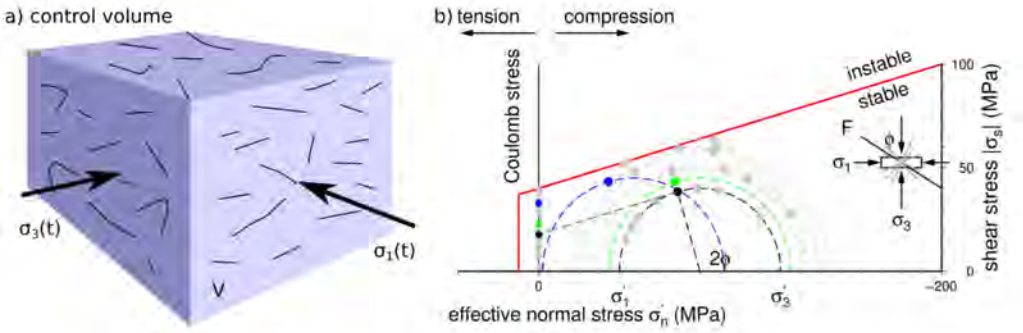

Figure 1. Conceptual sketch to derive an effective media approach for the distribution of faults or asperities sources in an effective media approach. (a) An infinite number of sources of different length and orientation are randomly distributed in a rock volume V. As some of them have experienced slip, and others not yet, the stress field in the rock volume is heterogeneous. (b) The Coulomb failure line is plotted in a Mohr stress diagram, where colored circles indicate the state of stress on individual faults. The heterogeneous stress in V was replaced by a substitute media with an effective, homogeneous stress. Each source is considered independently in the center of the rock volume with its orientation conserved. The Coulomb stress of each source, σ_c, aligns on the Coulomb stress axis. If the rock volume is externally loaded (dashed Mohr circles), the same stress change is assumed to apply to all sources in V and the σ_c is uniformly shifted on the Coulomb stress axis.

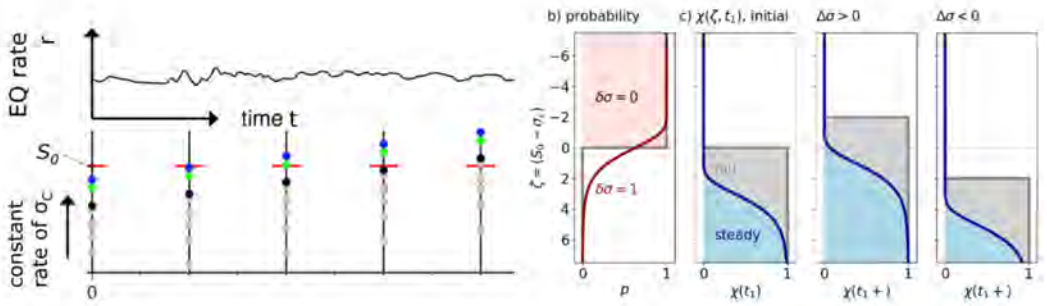

Figure 2. Schematic sketch to describe the implementation of time dependent stress loading and earthquake triggering. (a) The distribution of $\sigma_c^{(k)}$ on the Coulomb stress axis in Fig. 1b is plotted as a function of time assuming a uniform increase of stress stages at each asperity. A constant earthquake rate r is indicated. (b) Trigger probability function $p(\zeta)$. The linear Coulomb failure model assumes a step function trigger probability $p = H(\sigma - S_0) = H(-\zeta)$ (redish area, associated with $\delta\sigma = 0$). In the time-dependent model the probability is a smoothed function of a skin parameter $\delta\sigma$ (black line). (c) Normalized distribution of source stresses are defined by an initial susceptibility function $\chi(\zeta, t_1)$. The initial distributions at time t_1 for $\delta\sigma = 0$ are assumed uniform at $\zeta > 0$ (greyish area, CF model). For $\delta\sigma > 0$ the equilibrium distribution is a smooth function (bluish area). Due to stress loading or unloading, the distributions are shifted either shifted either to higher or lower levels on the stress axis with time.

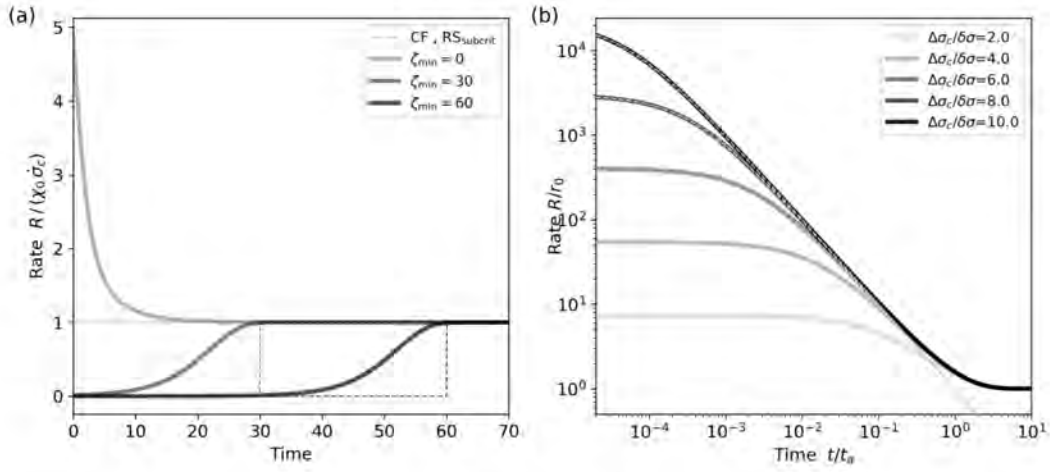

Figure 3. (a) Seismicity expected after the onset of a constant stressing rate $\dot{\sigma}_c$ at time 0 for a uniform pre-stress distribution $\chi(\zeta) = \chi_0 H(\zeta - \zeta_{\min})$. The curves refer to simulations which match Eq. (5). The model parameters are $\dot{\sigma}_c = t_0 = 1$ and $\delta\sigma = 5$. For comparison, the dashed lines show the correspondent (identical) forecasts of CF and $\mathrm{RS}_{\mathrm{subcrit}}$. (b) Relative seismicity rate increase R/r_0 following positive stress steps as a function of time in units of $t_a \equiv \delta\sigma/\dot{\sigma}_c$. Note that the curve shape only depends on $\Delta\sigma_c/\delta\sigma$. The lines refer to numerical simulations which match Eq. (7). For times $t \ll t_a$, the result is described by the Omori law (dashed curves) with $p = 1$ and K and c-values depending on the stress step according to Eq. (8).

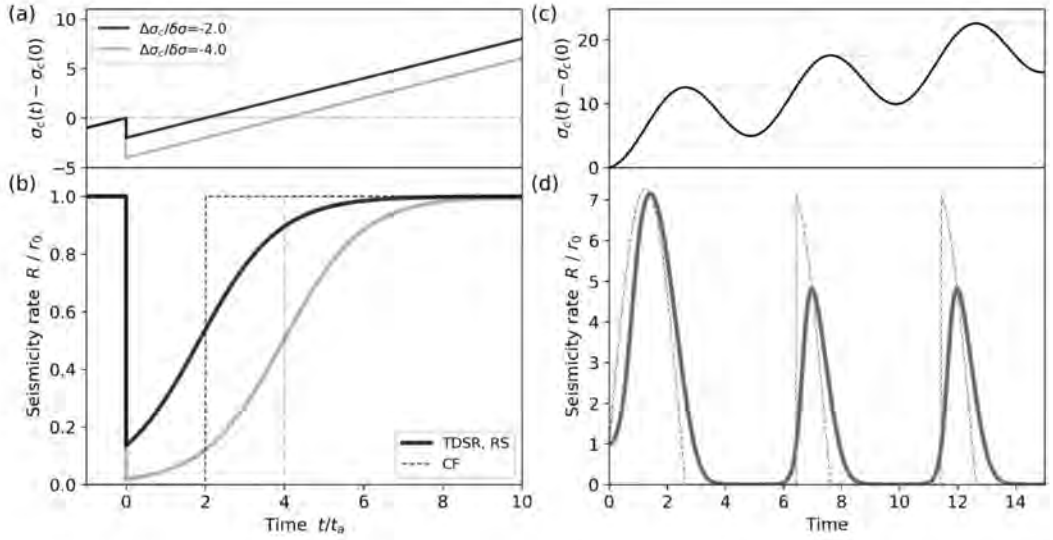

Figure 4. Rate decrease in response to a stress drop at time t=0 (a). As for positive stress steps, the rate simulations in (b) are also described for negative stress steps (here, $\Delta\sigma_c/\delta\sigma$=-2 and -4) by Eq. (7). (d) Seismicity response resulting from cyclic loading shown in (c) according to a cosine starting at time 0, where the model parameters are set to $\dot{\sigma}_c$=t_0=$\delta\sigma$=1. In all TDSR simulations, an initially constant seismicity rate and a constant background stressing rate is assumed. While the RS model predicts the same response in all cases, the CF model (dashed lines) predicts a total quiescence of length $t_a\,|\Delta\sigma_c|/\delta\sigma$ after the stress drop in (a-b) and during stress shadows marked by horizontal lines in (c).

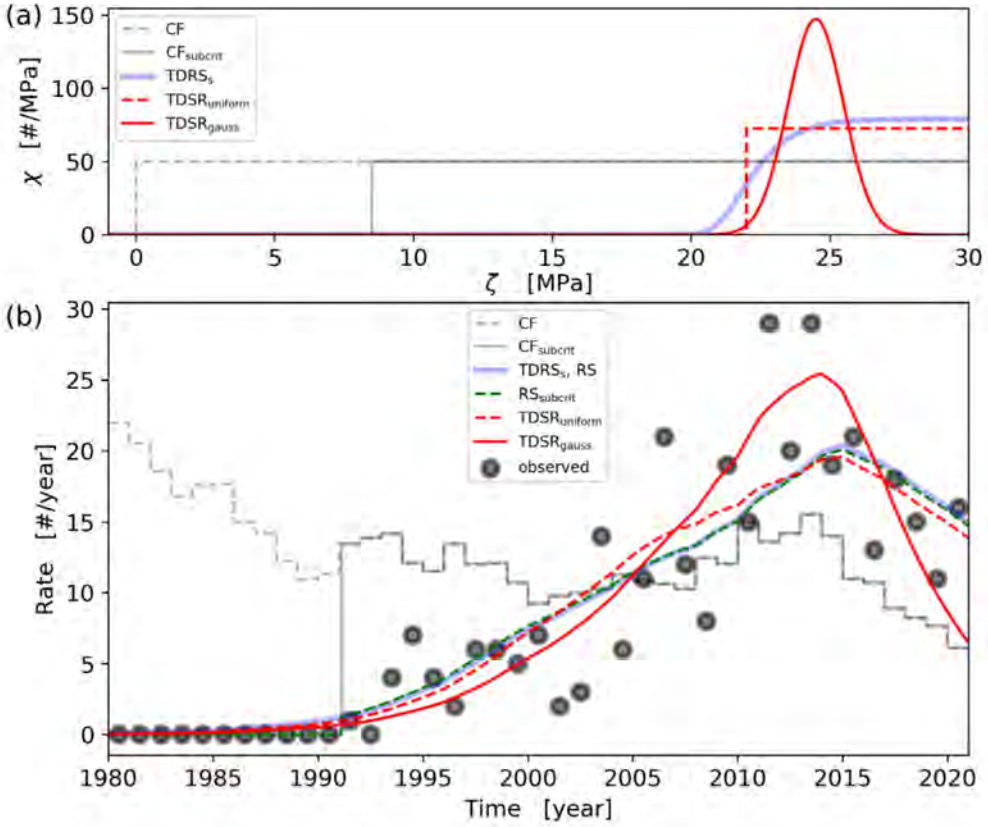

Figure 5. Application of the TDSR model to the Groningen gas field assuming different pre-stress distributions shown in (a): (i) stationary initial conditions ($TDSR_s$) corresponding to a background stressing rate of $\dot{\sigma}_c$=3.3 Pa/year, (ii) a uniform stress distribution of the sources for $\zeta > 22$ MPa ($TDSR_{uniform}$), and (iii) a Gaussian distribution with a mean of 24.5 MPa and a standard deviation of 1 MPa ($TDSR_{gauss}$). (b) The resulting seismicity response of the TDSR model to the mean pressure changes in the Groningen gas field, using t_0=10^{-4} years and $\delta\sigma$=1 MPa. Here, points refer to the annual rate of observed earthquakes with magnitudes larger than 1.45. For comparison, the corresponding curves are shown for the subcritical CF model ($CF_{subcrit}$) and the subcritical RS model of Heimisson et al. (2022) ($RS_{subcrit}$). In both cases, an initial stress gap was set to 8.5 MPa, reached just before the first observed earthquakes in 1991. In addition, a background stressing rate of $\dot{\sigma}_c$ = 17 kPa/year is assumed in $RS_{subcrit}$. Note that the RS model of Dieterich (1994) leads to an identical forecast as $TDSR_s$.

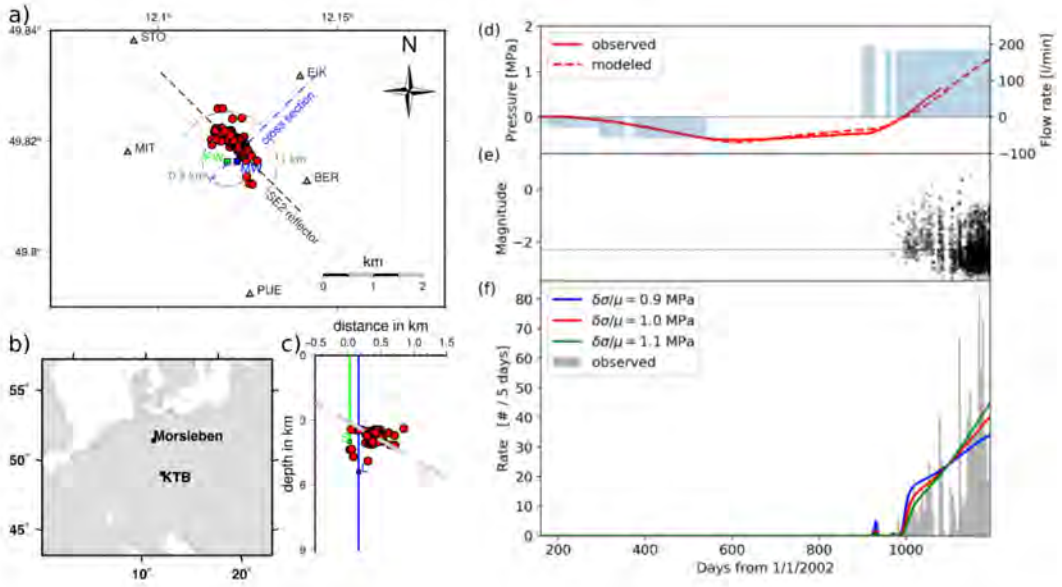

Figure 6. Longterm cyclic fluid production and injection experiment in crystalline rock at ∼4000 m depth in the pilot hole of the KTB drilling site. (a) Map view of the pilot (PW) and main well (MW), together with epicenters of earthquakes (red circles, $-1.8 \leq M_L \leq 1$) induced during the injection phase (Shapiro et al., 2006). (b) Overview map and (c) cross-section along the profile indicated in (a). (d) shows the injection rates (filled boxes), and measured (solid red) and predicted (dashed red) pore pressure at a depth of open section of the main well. (e) Occurrence of induced earthquakes and their magnitudes (taken from (Haney et al., 2011)). The dashed horizontal line indicates the selected magnitude of completeness, M_c=-2.3. (f) The observed earthquake rate ($m \geq -2.3$) is compared to TDSR predictions for $\dot{\sigma}_c = 30$ Pa/year and different values of $\delta\sigma/\mu$.

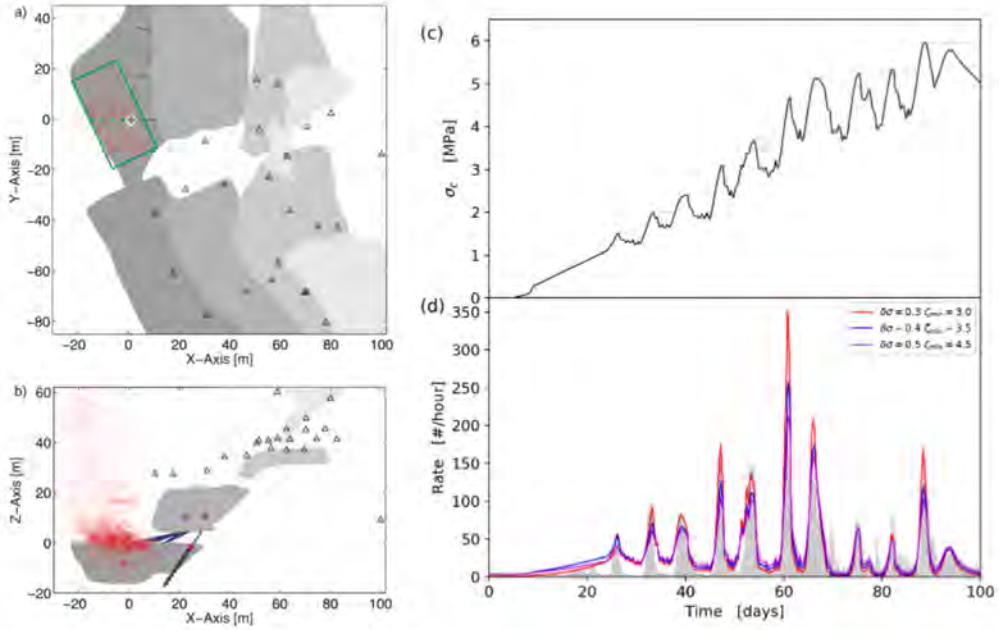

Figure 7. (a) Map view and (b) cross-section through the mine structure in Morsleben together with the seismic network of 24 piezoelectric sensors (triangles, sampling rate of 200 kHz) and the acoustic emissions (AE, red dots) (taken from (Becker et al., 2010)). The deepest gallery in (b) with the intense AE activity was affected by backfilling. The green rectangle in (a) indicates the volume in which AEs were selected for the analysis. The white circle indicates the position of the well where a temperature sensor chain was installed and used to model $\Delta\sigma_c$. (c) shows the Coulomb stress (solid line), where horizontal dashed lines indicate stress shadows. (d) compares the observed AE rates (gray shaded) with TDSR forecasts using different $\delta\sigma$ and $\zeta_{\min}$ values (see legend in units of MPa) and $t_0 = 0.01$d.

Appendix A Analytical derivations and simulation algorithm

A1 Derivation of the analytic solutions

Based on Eq. (4) the following cases can be analytically solved.

A11 Time evolution for an initially uniform χ in $[\zeta_{\min}, \infty]$

For the case that the initial state is uniformly distribution according to $\chi(\zeta) = \chi_0 H(\zeta - \zeta_{\min})$ and the volume is loaded with constant stressing rate $\dot{\sigma}_c$, the solution of Eq. (4) is given by

$$\chi(\zeta, t) = \chi_0 \, e^{-\frac{\delta\sigma}{t_0 \dot{\sigma}_c}\left(1 - e^{-\frac{\dot{\sigma}_c t}{\delta\sigma}}\right) e^{-\frac{\zeta}{\delta\sigma}}} \, H\left(\zeta + \dot{\sigma}_c t - \zeta_{\min}\right) \tag{A1}$$

Inserting this solution in Eq. (3) and solving the integral leads to

$$\begin{aligned} R(t) &= \frac{\chi_0}{t_0} \int_{\zeta_{\min} - \dot{\sigma}_c t}^{\infty} e^{-\frac{\delta\sigma}{t_0 \dot{\sigma}_c}\left(1 - e^{-\frac{\dot{\sigma}_c t}{\delta\sigma}}\right) e^{-\frac{\zeta}{\delta\sigma}}} \, e^{-\frac{\zeta}{\delta\sigma}} \, \mathrm{d}\zeta \\ &= \frac{\chi_0 \, \delta\sigma}{t_0} \frac{1 - e^{\frac{\delta\sigma}{t_0 \dot{\sigma}_c}\left(1 - e^{-\frac{\dot{\sigma}_c t}{\delta\sigma}}\right) e^{-\frac{\zeta_{\min} - \dot{\sigma}_c t}{\delta\sigma}}}}{\frac{\delta\sigma}{t_0 \dot{\sigma}_c}\left(1 - e^{-\frac{\dot{\sigma}_c t}{\delta\sigma}}\right)} \\ &= \chi_0 \dot{\sigma}_c \frac{1 - e^{\frac{\delta\sigma}{t_0 \dot{\sigma}_c}\left(1 - e^{-\frac{\dot{\sigma}_c t}{\delta\sigma}}\right) e^{-\frac{\zeta_{\min} - \dot{\sigma}_c t}{\delta\sigma}}}}{1 - e^{-\frac{\dot{\sigma}_c t}{\delta\sigma}}} \end{aligned} \tag{A2}$$

A12 Constant rate for constant loading

Here we consider the case that the rate is constant, i.e. $R(t) = r_0$, for given stressing rate $\dot{\sigma}_c$. In this case, the χ distribution is stationary, i.e. $\frac{\mathrm{d}}{\mathrm{d}t}\chi = 0$, and Equation (4) leads with $\frac{\mathrm{d}\zeta}{\mathrm{d}t} = -\dot{\sigma}_c$ to

$$\frac{\delta\chi}{\delta t} = \dot{\sigma}_c \frac{\delta\chi}{\delta\zeta} \tag{A3}$$

The solution has the general form

$$\chi(\zeta) = c \exp\left(-\frac{\delta\sigma}{t_0 \dot{\sigma}_c} e^{-\frac{\zeta}{\delta\sigma}}\right) \tag{A4}$$

The constant c is determined by the condition $R(t) = \int \chi(\zeta)/\bar{t}_f(\zeta) \, \mathrm{d}\zeta = r_0$, which yields $c = r_0/\dot{\sigma}_c$ considering that the integral of $\exp\left(-x - a\, e^{-x}\right)$ is equal to $\exp\left(-a\, e^{-x}\right)/a$, which is $1/a$ for $x \to \infty$ and 0 for $x \to -\infty$ given $a > 0$.

A13 Response to a stress step constant loading

Here we consider a stress step $\Delta\sigma_c$ at time $t = 0$ followed by a constant loading rate $\dot{\sigma}_{c,a}$ for a source population which was initially at steady state related to a background stressing rate $\dot{\sigma}_c$. In this case $\frac{\mathrm{d}\zeta}{\mathrm{d}t} = -\dot{\sigma}_{c,a}$ and Eq. (4) is equal to

$$\frac{\delta\chi}{\delta t} - \dot{\sigma}_{c,a}\frac{\delta\chi}{\delta\zeta} = -\chi / \bar{t}_f(\zeta) \tag{A5}$$

Given the initial condition $\chi(\zeta, 0) = \chi_s(\zeta + \Delta\sigma_c)$, the solution of this equation is given by

$$\chi(\zeta,t) = \frac{r_0}{\dot{\sigma}_c} e^{-\frac{\delta\sigma}{t_0\dot{\sigma}_{c,a}}\left[\left(\frac{\dot{\sigma}_{c,a}}{\dot{\sigma}_c}e^{-\frac{\Delta\sigma_c}{\delta\sigma}}-1\right)e^{-\frac{\dot{\sigma}_{c,a}\,t}{\delta\sigma}}+1\right]e^{-\frac{\zeta}{\delta\sigma}}} \tag{A6}$$

Inserting this solution in Eq. (3) and solving the integral leads to

$$\begin{aligned} R(t) &= \frac{r_0}{t_0\dot{\sigma}_c}\int_{-\infty}^{\infty} e^{-\frac{\delta\sigma}{t_0\dot{\sigma}_{c,a}}\left[\left(\frac{\dot{\sigma}_{c,a}}{\dot{\sigma}_c}e^{-\frac{\Delta\sigma_c}{\delta\sigma}}-1\right)e^{-\frac{\dot{\sigma}_{c,a}\,t}{\delta\sigma}}+1\right]e^{-\frac{\zeta}{\delta\sigma}}} e^{-\frac{\zeta}{\delta\sigma}}\,\mathrm{d}\zeta \\ &= \frac{r_0\delta\sigma}{t_0\dot{\sigma}_c}\left(\frac{\delta\sigma}{t_0\dot{\sigma}_{c,a}}\left[\left(\frac{\dot{\sigma}_{c,a}}{\dot{\sigma}_c}e^{-\frac{\Delta\sigma_c}{\delta\sigma}}-1\right)e^{-\frac{\dot{\sigma}_{c,a}\,t}{\delta\sigma}}+1\right]\right)^{-1} \\ &= \frac{r_0\,\frac{\dot{\sigma}_{c,a}}{\dot{\sigma}_c}}{\left(\frac{\dot{\sigma}_{c,a}}{\dot{\sigma}_c}e^{-\frac{\Delta\sigma_c}{\delta\sigma}}-1\right)e^{-\frac{\dot{\sigma}_{c,a}\,t}{\delta\sigma}}+1} \end{aligned} \tag{A7}$$

where it is again considered that the integral of $\exp(-x - a\,e^{-x})$ is equal to $\exp(-a\,e^{-x})/a$, which is $1/a$ for $x \to \infty$ and 0 for $x \to -\infty$ given $a > 0$.

A14 Response to a stress step without subsequent loading

For the specific case of $\dot{\sigma}_{c,a} = 0$, the solution of Eq. (8) can be achieved by expanding the exponential term $\exp(-\dot{\sigma}_{c,a}\,t\,/\,\delta\sigma)$ of Eq. (A7) in a Taylor series and consider the limit $\dot{\sigma}_{c,a} \to 0$.

A15 Change of stressing rate

For the case that at $t = 0$ the stressing rate changes $\dot{\sigma}_{c,a} \neq \dot{\sigma}_c$, the solution provided in Eq. (9) follows from setting $\Delta\sigma_c = 0$ in Eq. (A7).

A2 Algorithm

The model is implemented by the following algorithm:

1. Discretize stress evolution $\sigma_{c,i} = \sigma_c(t_i)$ at time steps t_i $(i = 1, \ldots, N)$

2. Initialize the distribution $\chi_{k,i}$ at $\zeta_{k,1} \in [Z_1, Z_2]$ $(k = 1, \ldots, M)$, where $Z_1 \ll -\delta\sigma$ and $Z_2 \gg \delta\sigma$ and larger than the maximum stress change $(\Delta\sigma_{c,max})$ to avoid finite-size effects. For our simulations, e.g., we chose $Z_1 = -Z$ and $Z_2 = Z$ with $Z = 10 \cdot \delta\sigma + \Delta\sigma_{c,max}$. In the case of initially subcritical stresses, the value of Z_2 should be further increased.
3. Set $i = 1$
4. Calculate total rate $R_i = \sum_k \left(\chi_{k,i} \,/\, \bar{t}_f(\zeta_{k,i})\right) \Delta\zeta$
5. Update ζ-values by $\zeta_{k,i+1} = \zeta_{k,i} + \sigma_{c,i} - \sigma_{c,i+1}$
6. Update χ-values by $\chi_{k,i+1} = \chi_{k,i} - \left(\chi_{k,i} \,/\, \bar{t}_f(\zeta_{k,i})\right) \cdot (t_{i+1} - t_i)$
7. Set $i = i + 1$ and repeat steps (4)-(7) until $i = N$

A python implementation of TDSR together with the RS and CF model is prepared under the open source github project https://github.com/torstendahm/tdsm.

Appendix B Mean failure times in the TDSR and RS models

The mean failure time for delayed fractures plays a key role in time-dependent brittle deformation and seismicity models. We use a exponential function (Eq. 2) that has been widely used to study subcritical crack growth and brittle failure in geological materials, both under tensional stresses (Aktinson, 1984) and compressional (shear) stresses (Scholz, 1968; Ohnaka, 1983), of the form

$$\bar{t}_f \;=\; a e^{E/KT} \cdot e^{(S_0 - \sigma_c)/b} \;= a e^{E/KT + S_0/b} \cdot e^{-\sigma_c/b} \tag{B1}$$

where a (unit [s]) and b (unit [Pa]) are constants and S_0 is the strength of the rock. For stress corrosion processes, E is the activation energy and K is the Boltzmann constant (Wiederhorn et al., 1980). In our model, we set $t_0 = a e^{E/KT}$ and $\delta\sigma = b$. A key point is that the mean time-to-failure is defined for a source under a given, absolute stress level σ_c, which is assumed constant.

In the RS model, a simplified spring slider model under friction is used. The nucleation process is characterized by an interval of self-driven, accelerated slip, which is used to define the time-to-failure by the time needed until the slip rate becomes very large or infinity. The time depends on constitutive parameters, the initial slip rate $\dot{\delta}_0$, and the stress level. Under constant Coulomb stress, the failure time is given by Eqs. A7 and

A14 in Dieterich (1994), i.e.,

$$\bar{t}_f \;=\; \frac{A}{H\dot{\delta}_0} = \frac{A}{H}\left\{\Pi f(\Theta_i)\right\}\cdot e^{-\sigma_c/A\sigma} \tag{B2}$$

where σ is the effective normal stress, and $\{\Pi f(\Theta)\}$ is a product of initial state variables. Furthermore, $H = \dfrac{B}{d_c} - \dfrac{k}{\sigma_0}$ with A and B constitutive parameters of the friction relation, k is the effective stiffness of the source patch, and d_c a characteristic slip distance over which states evolves (Dieterich, 1994). Note that RS assumes that normal stress remains approximately constant, and the product $A\sigma$ is taken as a model parameter. The solution (B2) is derived assuming that the stress level σ_c is kept constant. However, the derivation of seismicity rates in the RS model finally uses a time-independent solution for $\bar{t}_f$ for the case of a constant background stressing rate (Heimisson & Segall, 2018).

The form(B1) and (B2) can be directly compared. The mean fracture times are equal if $\delta\sigma = A\sigma$ and $t_0 e^{S_0/\delta\sigma} = \frac{A}{H}\left\{\Pi f(\Theta_i)\right\}$. It indicates that the mean time-to-failure for rate-and-state dependent frictional instabilities has the same form as the functions derived in lab experiments on brittle deformation and brittle failure. This similarity might explain why the TDSR and RS leads to the same analytic solutions for steady-state initial conditions, despite the very different model concepts.

Appendix C Open Research

The article presents a theoretical model, and all simulations are directly based on the corresponding theory. In the case of the real data examples, we used data from published work referenced in the paper. The TDSR model will be available as an open source python software tool under https://github.com/torstendahm/tdsm, where synthetic data examples can be reproduced.

Acknowledgments

We thank Dirk Becker for the processing data of the Morsleben mine application and Jörn Kummerow for providing locations and magnitudes for the KTB pumping and injection experiment.

References

Aktinson, B. (1984). Subcritical crack growth in geological materials. *J. Geophys. Res.*, *89*(B6), 4077-4114.

Becker, D., Cailleau, B., Dahm, T., Shapiro, S., & Kaiser, D. (2010). Stress triggering and stress memory observed from acoustic emissions records in a salt mine. *Geophys. J. Int.*, 10.1111/j.1365-246X.2010.0464.x.

Bourne, S., & Oates, S. (2017). Extreme threshold failures within a heterogeneous elastic thin sheet and the spatial-temporal development of induced seismicity within the Groningen gas field. *J. Geophys. Res., 122*, 10299–10320.

Bourne, S., Oates, S., & Van Elk, J. (2018). The exponential rise of induced seismicity with increasing stress levels in the Groningen gas field and its implications for controlling seismic risk. *Geophys. J. Int., 213*(3), 1693–1700.

Candela, T., Wassing, B., Ter Heege, J., & Buijze, L. (2018). How earthquakes are induced. *Science*, *360*(6389), 598–600.

Cattania, C., Hainzl, S., Wang, L., Roth, F., & Enescu, B. (2014). Propagation of Coulomb stress uncertainties in physics-based aftershock models. *J. Geophys. Res., 119*, 7846–7864.

Cattania, C., Werner, M. J., Marzocchi, W., Hainzl, S., Rhoades, D., Gerstenberger, M., ... Jordan, T. H. (2018). The forecasting skill of physics-based seismicity models during the 2010–2012 Canterbury, New Zealand, earthquake sequence. *Seismological Research Letters*, *89*(4), 1238–1250.

Dahm, T., & Becker, T. (1998). On the elastic and viscous properties of media containing strongly interacting in-plane cracks. *Pure appl. geophys., 151*, 1-16.

Dieterich, J. (1994). A constitutive law for rate of earthquake production and its application to earthquake clustering. *J. Geophys. Res., 99*. 2601-618.

Dieterich, J. (2007). Applications of Rate- and State-Dependent Friction to Models of Fault Slip and Earthquake Occurrence. *Treatise on Geophysics*, *4*, 107-129.

Grässle, W., Kessels, W., Kümpel, H., & Li, X. (2006). Hydraulic observations from a 1 year fluid production test in the 4000 m deep KTB pilot borehole. *Geofluids*, *6*, 8-23. doi: 10.1029/2007JB005497

Grigoli, F., Cesca, S., Rinaldi, A., Malconi, A., Lopez-Comino, J., Westaway, R., ... Wiemer, S. (2018). The November 2017 Mw 5.5 Pohang earthquake: A possible case of induced seismicity in South Korea. *Science*, 10.1126/science.aat2010.

Hainzl, S., Brietzke, G., & Zoeller, G. (2010). Quantitative earthquake forecasts resulting from static stress triggering. *J. Geophys. Res., 115, B11311*,

10.1029/2010JB007473.

Hainzl, S., & Christophersen, A. (2017). Testing alternative temporal aftershock decay functions in an ETAS framework. *Geophys. J. Int.*, *210*, 585–593. doi: 10.1093/gji/ggx184

Hainzl, S., Enescu, B., Cocco, M., Woessner, J., Catalli, F., Wang, R., & Roth, F. (2009). Aftershock modeling based on uncertain stress calculations. *J. Geophys Res.*, *114*(B5), 1–12.

Hainzl, S., Steacy, S., & Marsan, D. (2010). Seismicity models based on Coulomb stress calculations. *Community Resource for Statistical Seismicity Analysis*. doi: 10.5078/corssa-32035809

Haney, F., Kummerow, J., Langenbruch, C., Dinske, C., Shapiro, S., & Scherbaum, F. (2011). Magnitude estimation for microseismicity induced during the KTB 2004/2005 injection experiment. *Geophysics*, *76*, WC47–WC53. doi: 10.1190/GEO2011-0020.1

Heimisson, E. R., Einarsson, P., Sigmundsson, F., & Brandsdóttir, B. (2015). Kilometer-scale Kaiser effect identified in Krafla volcano, Iceland. *Geophys. Res. Lett.*, *42*, 7958–7965. doi; doi:10.1002/2015GL065680

Heimisson, E. R., & Segall, P. (2018). Constitutive law for earthquake production based on rate-and-state friction: Dieterich 1994 revisited. *J. Geophys. Res.*, *123*, 4141-4156. doi: 10.1029/(2018JB015656

Heimisson, E. R., Smith, J. D., Avouac, J.-P., & Bourne, S. J. (2022). Coulomb threshold rate-and-state model for fault reactivation: application to induced seismicity at groningen. *Geophys. J. Int.*, *228*, 2061–2072.

Kagan, Y., & Jackson, D. (1991). Seismic gap hypothesis: ten years after. *J. Geophys. Res.*, *96*, 21419-21431. doi: DOI:10.1029/91JB02210

Kagan, Y., & Jackson, D. (1995). New seismic gap hypothesis: five years after. *J. Geophys. Res.*, *100*, 3943-3959. doi: DOI:10.1029/94JB03014

Köhler, N., Spies, T., & Dahm, T. (2009). Seismicity patterns and variation of the frequency-magnitude distribution of microcracks in salt. *Geophys. J. Int.*, *179*(1), 489–499.

Kühn, D., Hainzl, S., Dahm, T., Richter, G., & Rodriguez, I. V. (2022). A review of source models to further the understanding of the seismicity of the Groningen field. *Netherlands Journal of Geosciences, in press*.

Kümpel, H., Erzinger, J., & Shapiro, S. (2006). Two Massive Hydraulic Tests Completed in Deep KTB Pilot Hole. *Scientific Drilling*, *3*, 40-42. doi: doi:10.2204/iodp.sd.3.05.2006

Mancini, S., Segou, M., Werner, M. J., & Cattania, C. (2019). Improving physics-based aftershock forecasts during the 2016–2017 Central Italy earthquake cascade. *J. Geophys. Res.*, *124*, 8626–8643.

Marsan, D., & Ross, Z. E. (2021). Inverse migration of seismicity quiescence during the 2019 ridgecrest sequence. *J. Geophys. Res.*, *126*, e2020JB020329.

Matthews, M., Ellsworth, W., & Reasenberg, P. (2002). A Brownian model for recurrent earthquakes. *Bull. Seism. Soc. Am.*, *92*(6), 2233-2250. doi: doi.org/10.1785/0120010267

Ogata, Y. (1988). Statistical models for earthquake occurrence and residual analysis for point processes. *J. Am. Stat. Assoc.*, *83*, 9-27.

Ohnaka, M. (1983). Acoustic Emission During Creep of Brittle Rock. *Int J. Rock Mech. Min. Sci. & Geomech.*, *20*, 121–134.

Ohnaka, M. (2013). *The Physics of Rock Failure and Earthquakes*. Cambridge University Press, Cambridge.

Passarelli, L., Hainzl, S., Cesca, S., Maccaferri, F., Mucciarelli, M., Roessler, D., ... Rivalta, E. (2015). Aseismic transient driving the swarm-like seismic sequence in the Pollino range, Southern Italy. *Geophys. J. Int.*, *201*(3), 1553-1567. doi: doi.org/10.1093/gji/ggv111

Passarelli, L., Maccaferri, F., Rivalta, E., Dahm, T., & Abebe Boku, E. (2013). A probabilistic approach for the classification of earthquakes as "triggered" or "not triggered": application to the 1975 Krafla diking event followed by the 13th Jan 1976 M 6.2 earthquake on the Tjörnes Fracture Zone, Iceland. *J. Seism.*, 10.1007/s10950-012-9289-4.

Perfettini, H., & Avouac, J.-P. (2004). Postseismic relaxation driven by brittle creep: A possible mechanism to reconcile geodetic measurements and the decay rate of aftershocks, application to the Chi-Chi earthquake, Taiwan. *J. Geophys. Res., 109, B02304*. doi: doi:10.1029/2003JB002488

Reid, H. F. (1911). The elastic rebound theory of earthquakes. *Bull. Dep. Geol. Univ. Calif.*, *6*, 412–444.

Richter, G., Hainzl, S., Dahm, T., & Zöller, G. (2020). Stress-based, statistical mod-

eling of the induced seismicity at the Groningen gas field, the Netherlands. *Environmental Earth Sciences*, *79*, 1–15.

Roth, F., Dahm, T., & Hainzl, S. (2017). Testing stress shadowing effects at the South American subduction zone. *Geophysical Journal International*, *211*(2), 1272-1283.

Rudnicki, J. (1986). Fluid mass sources and point forces in linear elastic diffusive solids. *Mechanics of Materials*, *5*, 383-393.

Ruina, A. (1983). Slip instability and state variable friction laws. *J. Geophys. Res.*, *88*(B12), 10,359–10,370.

Scholz, C. H. (1968). Mechanism of creep in brittle rock. *J. Geophys. Res.*, *73*, 3295-3302.

Scholz, C. H. (2015). On the stress dependence of the earthquake *b* value. *Geophys. Res. Lett.*, *42*, 1399–1402.

Shapiro, S., Kummerow, J., Dinske, C., Asch, G., Rothert, J., E. Erzinger, Kümpel, H., & Kind, R. (2006). Fluid induced seismicity guided by a continental fault: Injection experiment of 2004/2005 at the German Deep Drilling Site (KTB). *Geophys. Res. Lett.*, *33*, 10.1029/2005GL024659.

Utsu, T., Ogata, Y., & Matsut'ura, R. (1995). The centenary of the Omori formula for decay law of aftershock seismicity. *J.Phys. Earth*, *43*, 1-33.

Vere-Jones, D. (1978). Earthquake prediction – a statistician's view. *J. Phys. Earth*, *26*, 129–146.

Wiederhorn, H., Fuller, E., & Thomson, R. (1980). Micromechanics of crack growth in ceramics and glasses in corrosive environments. *Metal Science*, *14*, 450–458.

Woessner, J., Hainzl, S., Marzocchi, W., Werner, M. J., Lombardi, A. M., Catalli, F., ... Wiemer, S. (2011). A retrospective comparative forecast test on the 1992 Landers sequence. *J. Geophys Res.*, *116*(B5), 1–22.

Zoback, M., & Harjes, H.-P. (1997). Injection-induced earthquakes and crustal stress at 9 km depth at the KTB deep drilling site, Germany. *J. Geophys. Res.*, *102*, 18477-18491.